RSC Advances

PAPER

Cite this: *RSC Adv.*, 2016, **6**, 47459

Growth temperature-dependent performance of planar $CH_3NH_3PbI_3$ solar cells fabricated by a two-step subliming vapor method below 120 °C

Shuai Yuan,[a] Zhiwen Qiu,[a] Hailiang Zhang,[a] Xiaofeng Qiu,[a] Chaomin Gao,[a] Haibo Gong,[a] Shikuan Yang,[b] Jinhua Yu[a] and Bingqiang Cao*[a]

Received 24th March 2016
Accepted 27th April 2016

DOI: 10.1039/c6ra07686f

www.rsc.org/advances

Using an extremely simple but promising two-step sequential subliming vapor deposition method, we grow high-quality perovskite $CH_3NH_3PbI_3$ films with a uniform and continuous surface coverage. The perovskite film morphology and growth orientation can be well controlled by the growth temperature. The temperature influence on the power conversion efficiency (PCE) and the current–voltage hysteresis of the Spiro/$CH_3NH_3PbI_3$/TiO_2 P-i-N planar film solar cells is also investigated. Furthermore, a novel solvent annealed PCBM film was introduced between the TiO_2 compact layer and perovskite active layer, which not only reduces the *J*–*V* hysteresis obviously but also enhances device performance. After optimization of the fabrication temperature and device structure, it was found that the PCEs of the solar cells fabricated at 120 °C on glass and flexible PET substrates can reach 15.59% and 7.62%, respectively. This promising approach provides a way to construct low-cost and large-area perovskite cell devices.

1. Introduction

Solar energy is one of the most promising candidates to replace fossil fuel energy in the future. The past few years have witnessed a stunning development in the field of perovskite $CH_3NH_3PbX_3$ (X = Cl, Br, I) based solar cells. Several groups have demonstrated the fabrication of cells with high photovoltaic efficiencies,[1–14] which is due to the outstanding intrinsic physical properties of the perovskite materials including long charge carrier diffusion length, direct energy bandgap and large absorption coefficient.[15–19] The photovoltaic efficiency of the perovskite solar cell can even compete with that of the state-of-the-art single crystalline silicon based solar cells. The cost-effectiveness and the simple fabrication process further highlight the merits of perovskite solar cells. For this typical solar cell, perovskite material as a light absorber is embedded between the hole and electron transport layers with or without a mesoporous layer consisting of TiO_2, Al_2O_3 or ZrO_2.[2,4,7] The photovoltaic efficiency can be varied from 3.8% (ref. 1) to 20.8%,[19] determined by the homogeneity and continuity of the perovskite light absorber layer. Therefore, the preparation of a high-quality perovskite layer is of vital importance to improve the solar cell performance. Nowadays, the common processes to prepare perovskite films include one-step solution deposition,[2] a two-step sequential solution method,[6] and vapor-phase deposition.[7] However, the one-step method has shortcomings in film homogeneity and continuity, which inhibit the cell repeatability. The sequential deposition method needs a soaking reaction procedure that may cause the perovskite film to peel off because of long time immersion. Wu *et al.*[10] used the strongly coordinative solvent DMSO for the processing of PbI_2 to attain amorphous featured precursor films, which can efficiently generate uniform perovskite crystals with a full conversion. Anyway, the solution evaporation process involves inevitable uncertainties, which can be induced by the ambient conditions (*e.g.*, temperature, humidity, air turbulence, *etc.*) and the wetting properties of the substrates, giving rise to poor controllability and reliability.

Comparatively, the vapor phase deposition is more reliable.[7,8] Even though the equipment is relatively complicated and expensive, it is still a promising candidate to grow perovskite films on a large scale for industrial applications where reliable device performance is paramount. A few reformative vapor methods have also been employed to improve the quality of perovskite films.[20–24] For example, Chen *et al.*[20] and Du *et al.*[21] replaced the immersing procedure by moving the PbI_2 coated substrate into a MAI-rich N_2 atmosphere at 150–155 °C, which achieved high device performance. However, this vapor-assisted deposition method is still based on coating a lead halide precursor solution, which has no advantages in large size film growth. Matthew and co-workers prepared superb perovskite films with an extremely stable efficiency of 11.8% by employing a complex multi-zone hybrid chemical vapor deposition (CVD)

[a]*Laboratory of Inorganic Energy and Environment Materials, School of Material Science and Engineering, School of Chemistry and Chemical Engineering, University of Jinan, Jinan 250022, Shandong, China. E-mail: mse_caobq@ujn.edu.cn; Fax: +86-531-8973-6292; Tel: +86-531-8973-6292*

[b]*Department of Mechanical and Nuclear Engineering and Materials Research Institute, The Pennsylvania State University, University Park, PA 16802, USA*

method, which can be further developed as an industrial process to grow perovskite films at low cost.[22] Several growth parameters play key roles in the gas phase growth method, among which the growth temperature not only sways the reaction constant but also influences the film crystalline and physical qualities. Therefore, it is crucial to find the optimized growth temperature during vapor phase methods to improve the perovskite film quality and increase the cell device efficiency.

Herein, a simple low-temperature sequential subliming method is adopted to grow $CH_3NH_3PbI_3$ films with a uniform and continuous morphology, where the MAI sublimation reaction process and the annealing treatment could be simply controlled with the same temperature in an ambient atmosphere. We systematically studied the temperature influence on the microstructure of the perovskite films and the performance of their formed solar cells. It is found that the $CH_3NH_3PbI_3$ growth temperature plays a key role and influences film crystallinity, crystal orientation, optical properties, and, in turn, the final cell performance. Combining with interface modification, the optimized PCE can reach as high as 15.59% with neglected *J–V* hysteresis. The whole device fabrication procedure was carried out at a temperature of as low as 120 °C. As an example, flexible perovskite solar cells based on this simple low-temperature vapor phase deposition method were also fabricated. These results prove the importance of fabrication temperature in influencing the performance of perovskite solar cells and provide guidance for designing high performance perovskite solar cells using vapor deposition methods.

2. Experimental section

2.1 Materials

CH_3NH_3I was synthesized using the method reported in ref. 2. Briefly, 30 ml of methylamine (40% in methanol) was mixed with 32.3 ml of hydroiodic acid (57 wt% in water) in a round-bottom flask at 0 °C for 2 h with stirring. The solvent was removed by heating the solution in a rotary evaporator at 50 °C for 30 min. The white-yellow precipitates of raw CH_3NH_3I were washed with ethanol, filtered and then washed with diethyl ether again. This procedure was repeated three times. After the last filtration, the products were dried at 70 °C in a vacuum oven for 8 h.

2.2 Perovskite film growth and device fabrication

The devices were prepared on cleaned fluorine-doped tin oxide (FTO) substrates. FTO glass (20 Ω $\square^{-1}$) was first etched to form a strip of conductive area on the edge side by HCl and Zn powders. The etched substrates were then sequentially cleaned in soap water, acetone, deionized water, and ethanol in an ultrasonic bath, and then dried under nitrogen flow, followed by putting the cleaned FTO in a 0.2 M $TiCl_4$ solution at 70 °C for one hour to prepare the compact TiO_2 (c-TiO_2) blocking layer. For interface modification, a dual-electron transporting layer was introduced, phenyl-C_{61}-butyric acid methyl ester (PCBM, a fullerene derivative) dissolved in chlorobenzene with 20 mg ml^{-1} was deposited on the compact TiO_2 layer by spin-coating at 3000 rpm, which provided a uniform PCBM film of 15 nm. The PCBM/TiO_2 coated substrates were put onto a hot plate and covered by a glass Petri dish. 15 μl of the CB solvent was added at the edge of the Petri dish during the thermal annealing at a temperature of 100 °C for 30 min. Then, the PbI_2 film with a thickness of about 150 nm was deposited by vacuum thermal evaporation at an evaporation rate of 0.5 Å s^{-1} monitored by a quartz microbalance sensor. The as-grown PbI_2 films were fixed onto quadrate Al_2O_3 boat covers and the PbI_2-coated substrates were about 2 cm above the CH_3NH_3I powders with the PbI_2 side facing downward. Then, this boat was moved into a quartz tube furnace with the temperature controlled at 110 °C, 120 °C, 130 °C, and 140 °C, respectively, for an hour in air to grow the perovskite film, and the environmental humidity was controlled under 25%. Finally, possible redundant MAI powder was washed with isopropanol (IPA) and the as-grown samples were ready for characterization. The hole transporting layer was deposited by spin-coating a solution at 3000 rpm for 30 s composed of 72.3 mg Spiro-OMeTAD (Ningbo Borun), 28.8 μl of 4-*tert*-butylpyridine, and 17.5 μl of lithium-bis(trifluoromethanesulfonyl)imide (Li-TFSI) solution (520 mg in 1 ml of acetonitrile, all dissolved in 1 ml of chlorobenzene). Silver (Ag, 120 nm) back contacts were thermally evaporated onto the Spiro-OMeTAD layer at 1×10^{-6} Torr in a vacuum deposition chamber. The flexible devices were fabricated on an indium-doped tin oxide (ITO)/polyethylene terephthalate (PET) substrate. The PEDOT:PSS layer was casted on the top of ITO at 5000 rpm for 30 s. Then the substrates were annealed at 120 °C for 15 min, and the perovskite film was synthesized as above. The PCBM layer was spin-coated at 5000 rpm for 30 s from chlorobenzene with a concentration of 20 mg ml^{-1}. At last, silver (Ag, 120 nm) back contacts were thermally evaporated on the PCBM film at 1×10^{-6} Torr in a vacuum deposition chamber.

2.3 Device characterizations

Perovskite $CH_3NH_3PbI_3$ thin films for scanning electron microscopy (SEM), X-ray diffraction (XRD), optical absorption and steady photoluminescence measurements were prepared using the same growth conditions as for the solar cells. The SEM images were obtained using a Quanta FEG250 field emission scanning electron microscope. An X-ray diffractometer (D8-Advance, Bruker) was employed to characterize the crystalline properties of the $CH_3NH_3PbI_3$ films. The UV-visible (UV-Vis) optical absorption spectrum was measured with a Shimadzu UV-3600 spectrophotometer. Steady photoluminescence was excited with a 450 nm diode laser source. The solar cell current density *versus* voltage (*J–V*) characteristics were measured using a Keithley Source Meter 2612A in the dark or under AM 1.5G simulated solar illumination with an intensity of 100 mW cm^{-2} (San-Ei, calibrated by a NREL-traceable KG5 filtered silicon reference cell) with different scanning directions. The metal cathodes were measured with a mask and the device area was determined by the overlap of the metal electrodes. Accurate device areas (0.1 cm^2) were measured device-by-device using

a calibrated optical microscope. The incident-photon-to-current conversion efficiency (IPCE) was measured with a QEX10 photoresponse system (PV Measurement Inc.).

3. Results and discussion

Fig. 1(a) schematically demonstrates the simple two-step sequential subliming vapor deposition growth method. The SEM image and XRD spectrum in Fig. 1(b and c) show the smooth and uniform surface morphology of the thermally deposited PbI_2 layer with a preferential (001)-orientation. The transformation of PbI_2 to $CH_3NH_3PbI_3$ is realized by moving the as-grown PbI_2 film into a quartz tube furnace with CH_3NH_3I vapor at different temperatures for an hour. The formation of perovskite $CH_3NH_3PbI_3$ can be simply described as,

$$PbI_{2(s)} + MAI_{(g)} \Leftrightarrow MAPbI_{3(s)} \quad (1)$$

s and g mean the solid and gas phase, respectively. Obviously, the reaction highly depends on the concentration of MAI gas that is closely related to the growth temperature. So, it is necessary to investigate the temperature influence on the growth of $CH_3NH_3PbI_3$ films.

To optimize the reaction between PbI_2 and CH_3NH_3I, a series of temperatures was adopted. Fig. 2 reveals a prominent relationship between the growth temperature and the perovskite film quality by XRD and SEM study. The XRD pattern in Fig. 2(a) shows the typical diffraction peaks that can be well assigned to the perovskite $CH_3NH_3PbI_3$ film. But, an additional peak at 12.62° from the PbI_2 (001) plane indicates the presence of unreacted PbI_2 in the sample obtained at 110 °C. The corresponding SEM image of Fig. 2(b) reveals a heterogeneous and rough film with bumps on the surface due to the remaining PbI_2. Intriguingly, an interface between the $CH_3NH_3PbI_3$ film and unreacted PbI_2 film can be observed from the cross-section SEM image (inset).

Fig. 2(c and d) show the XRD spectrum and SEM image of the perovskite film grown at 120 °C for one hour. Only the main diffraction peaks at 14.12° and 28.52° assigned to the $CH_3NH_3PbI_3$ (110) and (220) planes can be observed in Fig. 2(c). CH_3NH_3I and PbI_2 residuals are not detected, which indicates a high level of phase purity with a tetragonal crystal structure. Moreover, the highly (110)-oriented pure $CH_3NH_3PbI_3$ film demonstrates excellent crystallinity. Fig. 2(d) shows the corresponding homogeneous and uniform perovskite film without a pinhole in the entire scope of the top surface SEM image. This phenomenon draws our attention because all the $CH_3NH_3PbI_3$ grain boundaries cross the entire vertical scope from the bottom to the surface, and the average grain sizes of the 120 °C film are always slightly larger or comparable to the film thicknesses. This should greatly enhance the charge extraction process because the photogenerated carriers do not need to pass any grain boundaries during their transport in the out-of-plane direction before being collected by the electrodes. As shown in Fig. 2(e–h), the samples grown at 130 °C and 140 °C have lost the highly oriented growth behavior compared with the film grown at 120 °C. Meanwhile, the reduced grain diameters can be observed, and rough surface morphologies occupy

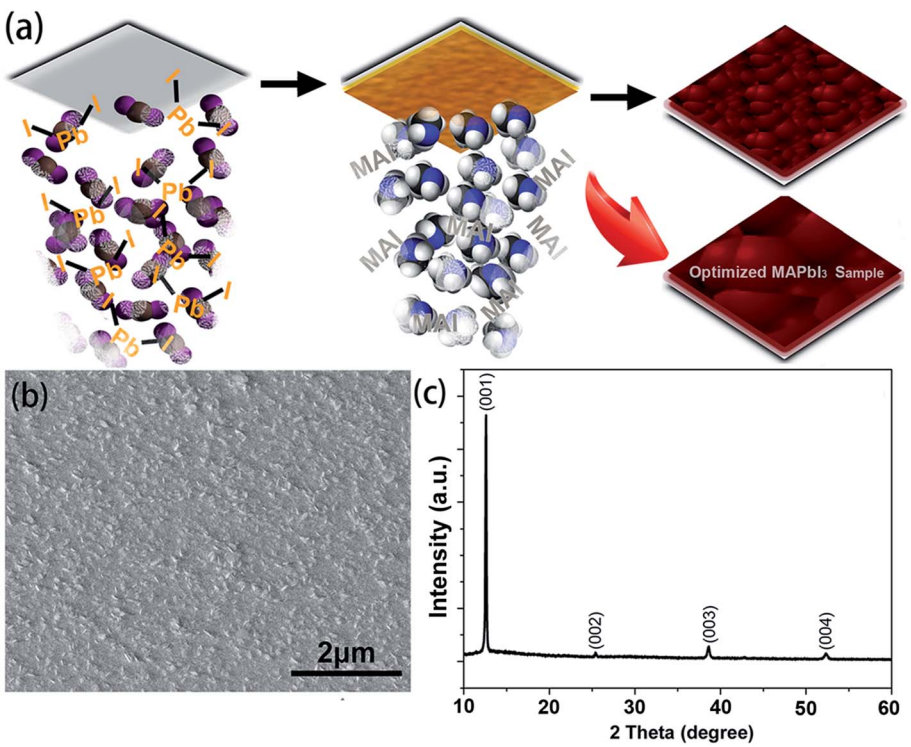

Fig. 1 (a) The schematic diagram of the two-step sequential vacuum subliming deposition growth method. (b) Surface SEM image of the thermal deposited PbI_2 film and (c) its corresponding XRD spectrum showing clear (001)-orientation.

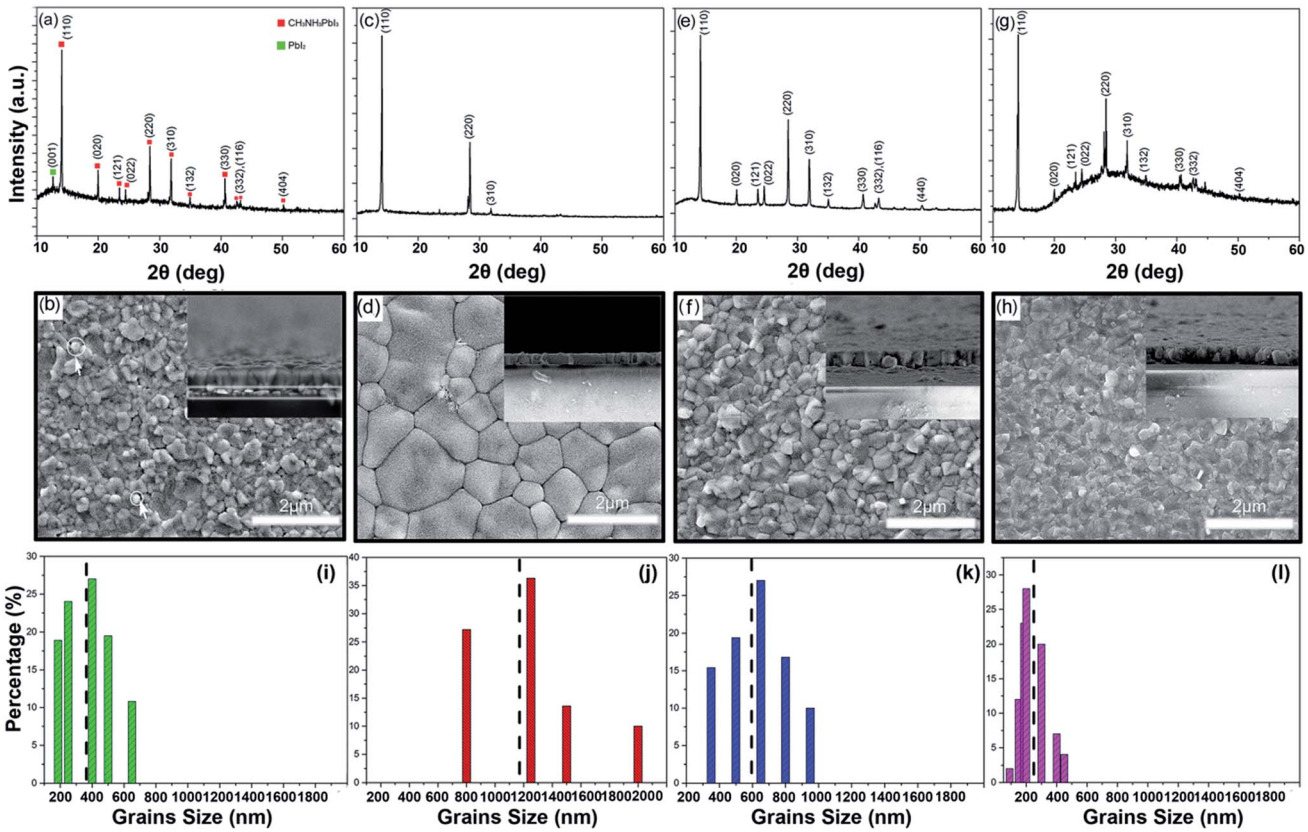

Fig. 2 XRD spectra and corresponding surface and cross-sectional (insets) SEM images of $CH_3NH_3PbI_3$ films synthesized at different growth temperatures: (a and b) 110 °C; (c and d) 120 °C; (e and f) 130 °C; (g and h) 140 °C. (i–l) Film grain size distributions calculated from the above SEM images and the average grain sizes marked with black vertical dash lines.

the entire films. With the Scherrer formula, we can estimate the grain size of the formed perovskite film but with large errors (not shown here). Instead, the grain-size distributions were calculated from the corresponding SEM images and the average grain sizes marked with black vertical dash lines are shown in Fig. 2(i–l). Clearly, the film grain size at 120 °C is bigger than the others.

An appropriate growth temperature (120 °C) along with proper MAI gas concentration will provide optimized growth conditions, where the film growth rate permits grain growth *via* oriented attachment.[25] This results in the grain distribution shifting to a larger size. The higher MAI gas concentration caused by higher reaction temperature, *e.g.* 130 °C and 140 °C, induces more random nucleation sites instead of enhancing the grain growth. Smaller grain size with increasing growth temperature is a clear trend, which is consistent with the SEM images as shown in Fig. 2. In contrast, lower growth temperature (110 °C) not only reduces MAI gas concentration but also decreases the gas molecule kinetic energy and substrate temperature, which prevents MAI gas from penetrating into the precursor film. In this scenario, the nucleation barrier potential impacts grain growth severely and incomplete growth and small grain size are observed.

Fig. 3(a) compares the optical absorption spectra of the PbI_2 film and the $CH_3NH_3PbI_3$ films grown at different temperatures. Two remarkable absorption edges at 800 nm for the $CH_3NH_3PbI_3$ film and 550 nm for the PbI_2 film are observed, which further confirms the feasibility of this growth method. The solely absorption edge indicates a direct energy bandgap of $CH_3NH_3PbI_3$ with a calculated value of 1.56 eV, which agrees well with a previous report.[4] Both the high absorption characteristics crossing all over the wavelength region from ultraviolet to 800 nm and the extremely high value in the short wavelength range demonstrate the excellent optical quality of the $CH_3NH_3PbI_3$ films except the sample prepared at 110 °C due to the incomplete reaction between the MAI and PbI_2. The normalized absorption spectrum of the 120 °C film (inset of Fig. 3(a)) exhibits a large slope and sharp band edge, indicating a better-ordered microstructure and lower electronic disorder compared with other films.[26]

Fig. 3(b) shows the steady-state PL spectra of perovskite films synthesized on glass substrates at varying temperatures, *e.g.* 110 °C, 120 °C, 130 °C, and 140 °C. Each PL spectrum presents a single Gaussian-shaped peak at about 760 nm, in good agreement with the near bandgap electron–hole recombination. The normalized PL spectra (Fig. 3(b), inset) have similar full width at half maximum. But, with growth temperature increasing, a minor PL peak shift towards the low energy direction was observed. We attribute this peak shifting to the subband states or shallow trap states. Moreover, the PL

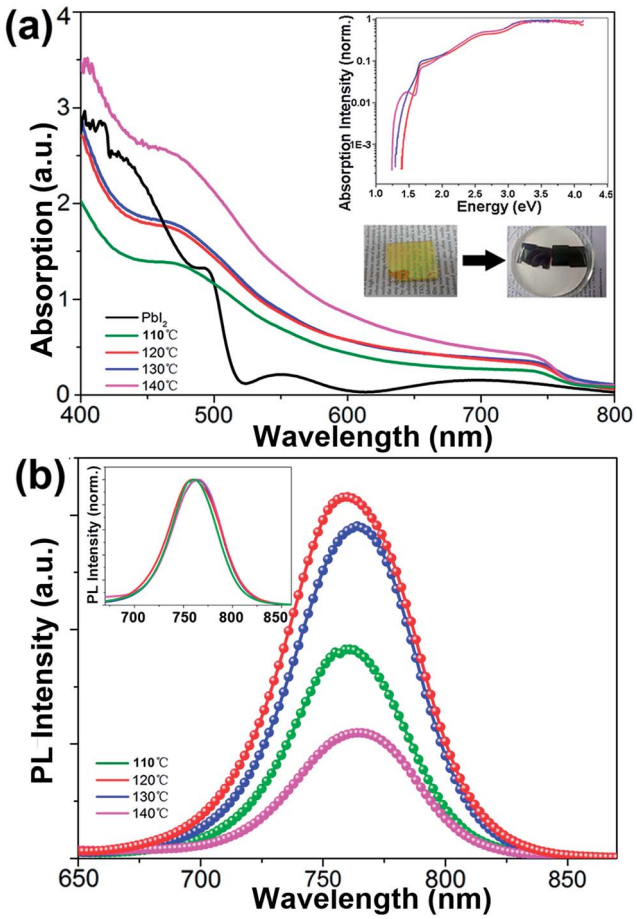

Fig. 3 (a) Optical absorption spectra of PbI_2 and $CH_3NH_3PbI_3$ films obtained at different temperatures, 110–140 °C. Insets are normalized absorption spectra of perovskite films and optical photographs of PbI_2 and $CH_3NH_3PbI_3$ films. (b) Photoluminescence and normalized photoluminescence spectra (inset) of $CH_3NH_3PbI_3$ films grown at different temperatures.

intensity from the sample grown at 120 °C is the strongest. Dane *et al.*[27] reported that higher perovskite film growth temperature results in larger trap density, which leads to a slight red-shifting of PL peaks and lower PL intensity. The stronger PL intensity at 120 °C indicates that the non-radiative decay is significantly suppressed due to its high crystal quality with reduced defects and electronic disorder.

Fig. 4(a) shows the cross-section SEM image of a complete solar cell device with the structure of FTO-glass/c-TiO_2/$CH_3NH_3PbI_3$/Spiro-OMeTAD/Ag. To fabricate such a structure, 50 nm of the c-TiO_2 electron transport layer was synthesized on a commercially available FTO glass substrate. The light absorber, $CH_3NH_3PbI_3$ film, was then grown with the above sequential subliming vapor deposition method. Then Spiro-OMeTAD was spin-coated as HTM before the thermal deposition of silver contacts. The as-grown perovskite film remains flat with an average film thickness of 350 nm.

The perovskite film growth temperature also has an important influence on their final photovoltaic performances. Fig. 4(b) shows the *J–V* characteristics of the perovskite solar cells with $CH_3NH_3PbI_3$ films grown at different temperatures. The fabrication procedures were kept the same for all cells except for the growth temperature of the perovskite films. The *J–V* characteristics deliver a short circuit current density (J_{sc}) of 16 mA cm^{-2}, an open circuit voltage (V_{oc}) of 1.10 V and a fill factor of 65% for the device fabricated at 120 °C. In contrast, the sample synthesized at 110 °C exhibits a smaller J_{sc} of 7.3 mA cm^{-2} and V_{oc} of 0.91 V caused by the incomplete reaction. It is reasonable to imagine that a PbI_2 film with high resistance and large energy band gap provides a potential barrier between the perovskite and TiO_2 electron transport layer, which leads to a negative effect on the built-in potential formation and electron extraction. Meanwhile, the poor light absorption properties of the perovskite film also induces the inferior performance. To further demonstrate the influence of different reaction temperatures, 31 separate devices from 4 batches were fabricated and measured. Fig. 4(c) reveals the average fill factor, open circuit voltage and short circuit current density of various batches, which demonstrate a close connection between the growth temperature and each cell parameter. Fig. 4(d) shows that with the reaction temperature increasing (over 120 °C), the average PCE decreased obviously. With an average efficiency of 10.37%, the cell of 120 °C triumphs over other groups. We attribute this trend to the improved crystal and physical qualities of the perovskite films. With the better $CH_3NH_3PbI_3$ film synthesized at 120 °C, the average J_{sc} of the batch exceed 16 mA cm^{-2} and the average fill factor is about 70%. Notably, the average V_{oc} over 1.05 V is higher than a previous report.[20] The large film grains with reduced defects and the uniform microstructure in the vertical direction over the range of the photocarrier diffusion length scale (100 nm to 1 μm for $CH_3NH_3PbI_3$) help to alleviate the recombination.

To further investigate the relationship between the solar cell performance and the perovskite film quality, the *J–V* characteristics of the devices were analyzed in Fig. 5. For devices with a large shunt resistance, the *I–V* characteristics of a solar cell can be described as,

$$J = J_L - J_0 \exp\left(\frac{q(V + J \times R_s)}{Ak_BT} - 1\right) \quad (2)$$

where J means the current flow through the external circuit, J_L is photogenerated current, J_0 is reverse saturated current density, A is the ideality factor, k_B is the Boltzmann constant, V is applied voltage, R_s is series resistance, for formula (2), it can be deduced as,

$$-\frac{dV}{dJ} = \frac{Ak_BT}{q}(J_{sc} - J)^{-1} + R_s \quad (3)$$

and

$$\ln(J_{sc} - J) = \frac{q}{Ak_BT}(V + R_s \times J) + \ln J_0. \quad (4)$$

The reverse saturated current J_0 can be gained from fitting the curve of $\ln(J_{sc} - J)$ *vs.* $q(V + R_s \times J)/Ak_BT + \ln J_0$. The plots of $-dV/dJ$ *vs.* $(J_{sc} - J)^{-1}$ and $\ln(J_{sc} - J)$ *vs.* $(V + R_s \times J)$ are shown in Fig. 5(a and b), respectively. Linear plot fitting of Fig. 5(a) shows

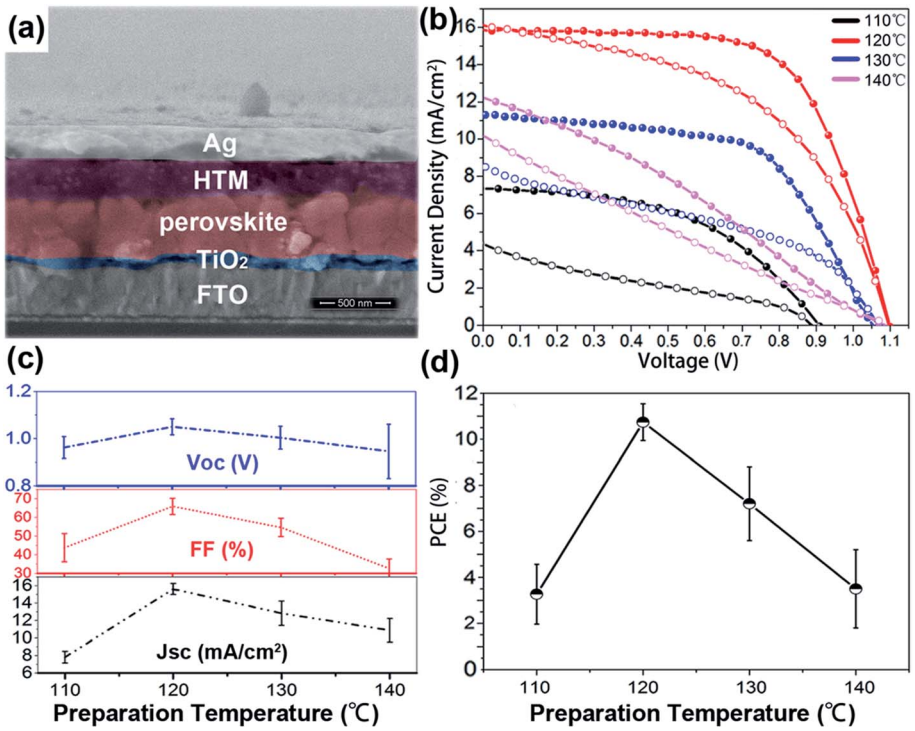

Fig. 4 (a) Cross-sectional SEM image of a typical solar cell showing the FTO-glass/c-TiO_2/$CH_3NH_3PbI_3$/Spiro-OMeTAD/Ag device structure. (b) *J*–*V* curves measured at different scanning directions (sphere for reverse and loop for forward) of the solar cells with $CH_3NH_3PbI_3$ light absorber films grown at different temperatures. (c and d) Average FF, V_{oc}, J_{sc}, and corresponding PCE of different groups of the perovskite solar cells, the device photovoltaic parameters are adopted from reverse scanning.

that the solar cell with the perovskite film synthesized at 120 °C exhibits the smallest series resistance, about 2.7 Ω cm^2. The series resistance values of the 130 °C and 140 °C devices are 5 and 10.7 Ω cm^2, respectively. The J_0 values for the 130 °C and 140 °C devices are 1.8×10^{-2} and 9.1×10^{-5} mA cm^{-2}, respectively. The J_0 from the 120 °C sample is as small as 1.2×10^{-5} mA cm^{-2}. J_0 is considered as a characteristic parameter directly related to the interface/bulk recombination rate. The small J_0 of the 120 °C device indicates a lower recombination loss, and, accordingly, a higher V_{oc} consistent with the measured high FF.

It is worth noting that planar perovskite solar cell devices have also been shown to be more susceptible to hysteresis effect,[28,29] as shown in Fig. 4(b) and 6(a), which is usually attributed to ionic displacement,[30] electronic carrier trapping,[31] or ferroelectric effects.[32] To quantify the hysteresis effect, the hysteresis index (H-index) is defined by the following equation,[33]

$$\text{H-index} = \frac{J_{\text{scan}}\left(\frac{-V_{\text{oc}}}{2}\right) - J_{\text{scan}}\left(\frac{+V_{\text{oc}}}{2}\right)}{J_{\text{scan}}\left(\frac{-V_{\text{oc}}}{2}\right)} \quad (5)$$

where $J_{\text{scan}}(-V_{oc}/2)$ is the photocurrent density at $V_{oc}/2$ bias for the reverse scan, while $J_{\text{scan}}(+V_{oc}/2)$ is the photocurrent density at $V_{oc}/2$ for the forward scan. A lower value of the hysteresis index means the cells have a weak hysteresis effect. In Fig. 6(a), we have plotted the hysteresis index values for different types of solar cells with $CH_3NH_3PbI_3$ active layers grown at different temperatures. Specially, the perovskite solar cells based on the $CH_3NH_3PbI_3$ layers grown at 120 °C exhibit smaller hysteresis than other cells. A similar tendency was observed for the $CH_3NH_3PbI_3$ solar cells with mesoporous TiO_2 as the electron transporting layer. The possible reason for this is the time-dependent photocurrent response attributed to the capacitive current related to the perovskite crystal size.[29] The operational stabilities of the cell were monitored by measuring the photocurrent densities at an applied bias close to the initial maximum power point ($V_{mp} \sim 0.85$ V) as a function of time as presented in Fig. 6(b and c). During a 1000 second illumination period, the unsealed cell shows a very stable photocurrent density and PCE as a function of time. A long-time operational stability study including aging tests under different relative humidity should be performed in future.

To further reduce the recombination of photocarriers at the electron extraction interface, correlative modification was also investigated in this work by employing a dual-electron transport layer consisting of PCBM and TiO_2. It should be noted that the PCBM modified layer was deposited using a novel solvent annealing process, which is confirmed to reduce the energy disorder of the PCBM film.[34] As shown in Fig. 7(a), the best modified perovskite device with a FTO/TiO_2/PCBM/$CH_3NH_3PbI_3$/Spiro/Ag structure has a short-circuit photo-current of 19.8 mA cm^{-2}, an open-circuit

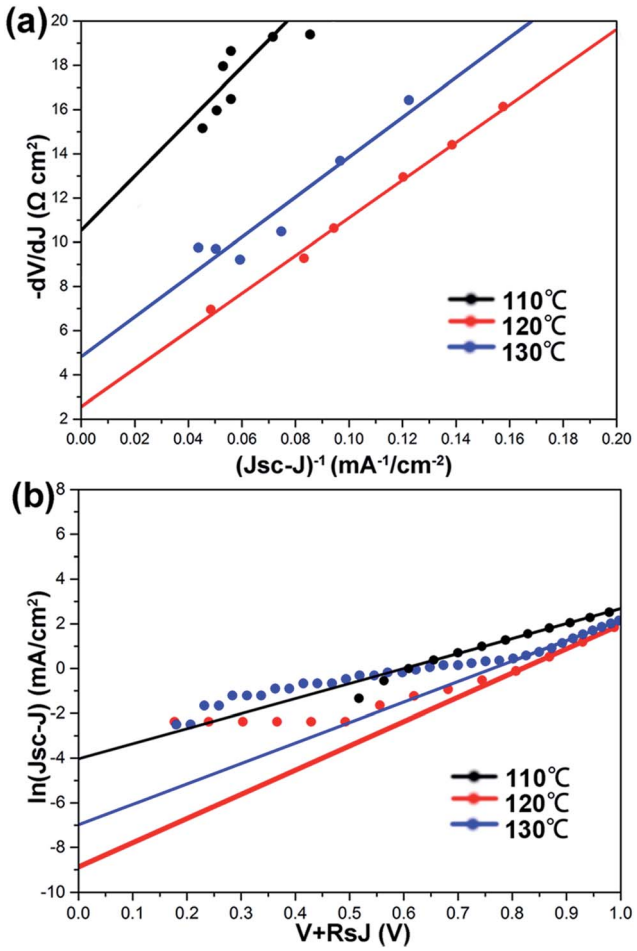

Fig. 5 I–V characteristics analyses. The original J–V curves and device performance parameters were shown in Fig. 4(b). (a) Plot of $-\mathrm{d}V/\mathrm{d}J$ *vs.* $(J_{sc} - J)^{-1}$ and the linear fitting; (b) $\ln(J_{sc} - J)$ *vs.* $(V + R_sJ)$ and the linear fitting.

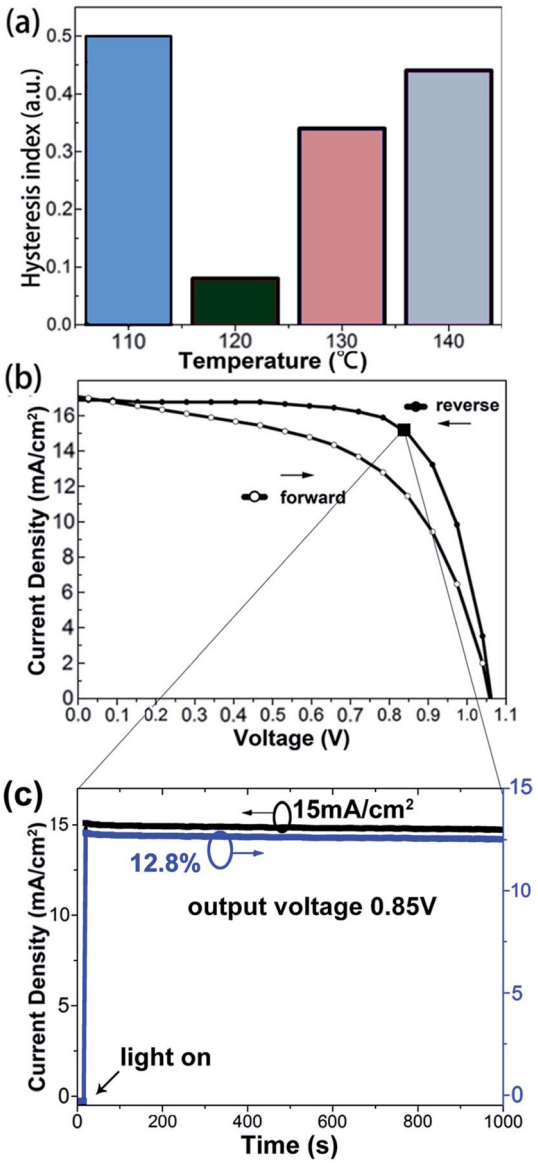

Fig. 6 (a) Bar graph showing the hysteresis index for solar cells with $CH_3NH_3PbI_3$ active layer grown at various temperatures. (b) The influence of scanning direction on the J–V characteristics of a typical solar cell with perovskite $CH_3NH_3PbI_3$ layer grown at 120 °C. J–V curves from V_{oc} to J_{sc} (reverse) or from J_{sc} to V_{oc} (forward) were measured under same conditions; the step voltage was 250 mV without delay time per step. (c) Steady-state photocurrent output at the maximum output point (0.85 V) and the corresponding PCE.

voltage of 1.01 V and a fill factor of 77.3%, yielding a PCE of 15.59%. Meanwhile, the hysteresis effect in this device is almost eliminated, and we attribute it to defect passivation and the superior electron transporting properties of the annealed PCBM layer.[35,36] Fig. 7(b) shows the corresponding EQE spectrum. The integral photocurrent from the EQE spectrum is 19.51 mA cm^{-2}, which is similar to the experimentally obtained J_{sc} of 19.8 mA cm^{-2}. The EQE value can reach 80% in the wavelength range from 400 nm to 600 nm. At last, such a low temperature device fabrication process was adopted for fabricating flexible perovskite solar cells. As the solution of $TiCl_4$ with a certain acidity leads to corrosion of the ITO film, we fabricate the devices with an inverted structure in which PEDOT:PSS(4083) and PCBM are employed as the hole transporting layer and electron transporting layer respectively. As can be seen from Fig. 7(c), the device on the ITO/PET substrate is flexible. The J–V curve of the highest-performing device on a flexible substrate is shown in Fig. 7(d), which yields a V_{oc} of 0.837 V, a J_{sc} of 14.7 mA cm^{-2}, a fill factor of 61.3%, and a PCE of 7.62%.

4. Conclusions

In conclusion, we have demonstrated a simple but promising two-step sequential subliming deposition method to synthesize $CH_3NH_3PbI_3$ films at an optimal growth temperature of 120 °C, by which we obtain high-quality perovskite films with a uniform surface, preferred orientation and reduced defect traits. The growth temperature-dependent performance of the planar $CH_3NH_3PbI_3$ solar cells was investigated in detail and benefiting from interface modification, the resulting best photovoltaic efficiency is as high as 15.59% with negligible

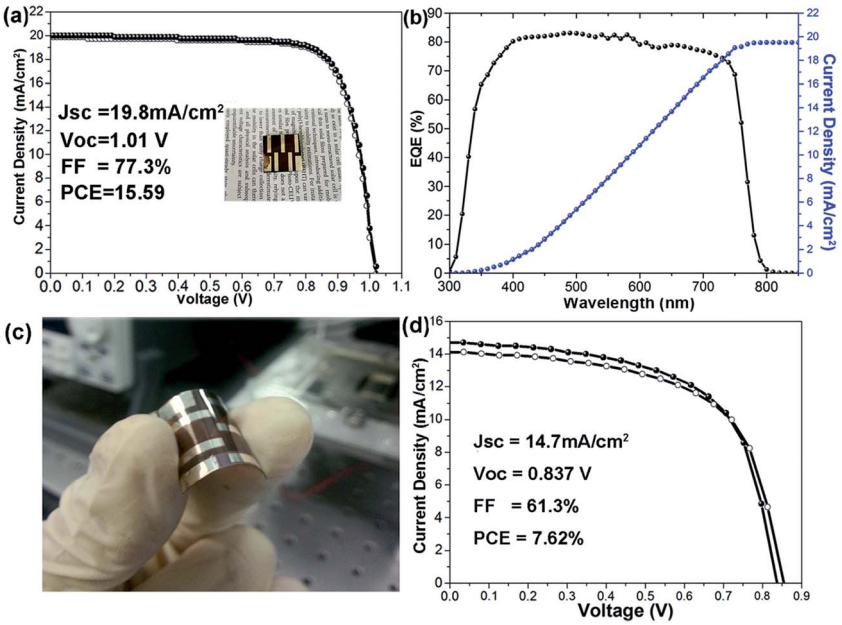

Fig. 7 (a) *J–V* characteristic curves of the modified dual-electron transport layer perovskite solar cell with perovskite film grown at 120 °C, sphere and loop lines for reverse and forward scanning, respectively. (b) The corresponding EQE spectrum of the device in (a). (c) The optical photograph of a flexible solar cell device on a PET substrate. (d) *J–V* curves of a flexible device with $CH_3NH_3PbI_3$ active layer grown at 120 °C, sphere and loop lines for reverse and forward scanning, respectively.

hysteresis. Moreover, all the fabrication of our perovskite solar cell can be conducted at temperatures as low as 120 °C, which can also be applied to flexible solar cell devices. Our findings emphasize the importance of fabrication temperature in preparing high performance perovskite solar cells and provide guidance for the future design of perovskite solar cells using vapor deposition methodologies.

Acknowledgements

This work is supported by the NSFC (51472110, 11174112) and Shandong Provincial Natural Science Foundation (JQ201214, 2014ZR01A47). The research program from the Ministry of Education, China, is also acknowledged (213021A). BC thanks the Taishan Scholar Chaired Professorship tenured at the University of Jinan.

Notes and references

1 A. Kojima, K. Teshima, Y. Shirai and T. Miyasaka, *J. Am. Chem. Soc.*, 2009, **131**, 6050–6051.
2 S. D. Stranks, G. E. Eperon, G. Grancini, C. Menelaou, M. J. P. Alcoaer, T. Leijtens, L. M. Herz, A. Petrinzza and H. J. Snaith, *Science*, 2013, **342**, 341–344.
3 L. K. Ono, S. H. Wang, Y. Kato, S. R. Raga and Y. B. Qi, *Sol. Energy Environ. Sci.*, 2014, **7**, 3989–3993.
4 H.-S. Kim, C.-R. Lee, J.-H. Im, K.-B. Lee, T. Moehl, A. Marchioro, S.-J. Moon, R. Humphry-Baker, J.-H. Yum, J. Moser, M. Grätzel and N.-G. Park, *Sci. Rep.*, 2012, **2**, 591.
5 J. H. Heo, S. H. Im, J. H. Noh, T. N. Mandal, C.-S. Lim, J. A. Chang, Y. H. Lee, H.-J. Kim, A. Sarkar, M. K. Nazeeruddin, M. Grätzel and S. I. Seok, *Nat. Photonics*, 2013, **7**, 486–491.
6 J. Burschka, N. Pellet, S.-J. Moon, R. Humphry-Baker, P. Gao, M. K. Nazeeruddin and M. Grätzel, *Nature*, 2013, **499**, 316–319.
7 M. Liu, M. B. Johnston and H. J. Snaith, *Nature*, 2013, **501**, 395–398.
8 C. Gao, J. Liu, C. Liao, Q. Y. Ye, Y. Z. Zhang, X. L. He, X. W. Guo, J. Mei and W. Lau, *RSC Adv.*, 2015, **5**, 26175–26180.
9 G. Sfyria, C. V. Kumar, D. Raptisa, V. Dracopoulos and P. Lianos, *Sol. Energy Mater. Sol. Cells*, 2015, **134**, 60–63.
10 Y. Z. Wu, A. Islam, X. D. Yang, C. J. Qin, J. Liu, K. Zhang, W. Q. Peng and L. Y. Han, *Energy Environ. Sci.*, 2014, **7**, 2934–2938.
11 O. Malinkiewicz, A. Yella, Y. H. Lee, G. M. Esoallargas, M. Grätzal, M. K. Nazeeruddin and H. J. Bolink, *Nat. Photonics*, 2014, **8**, 128–132.
12 N. Pellet, P. Gao, G. Gregori, T. Y. Yang, M. K. Nazeeruddin, J. Maier and M. Grätzel, *Angew. Chem., Int. Ed.*, 2014, **53**, 3151–3157.
13 H. P. Zhou, Q. Chen, G. Li, S. Luo, T. B. Song, H. S. Duan, Z. R. Hong, J. B. You, Y. S. Liu and Y. Yang, *Science*, 2014, **345**, 543–546.
14 W. S. Yang, J. H. Noh, N. J. Jeon, Y. C. Kim, S. Ryu, J. Seo and S. I. Seok, *Science*, 2015, **348**, 1234–1237.
15 G. Hodes, *Science*, 2013, **342**, 317–318.
16 N. G. Park, *J. Phys. Chem. Lett.*, 2013, **4**, 2423–2429.
17 H. S. Kim, S. H. Im and N. G. Park, *J. Phys. Chem. C*, 2014, **118**, 5615–5625.

18 G. C. Xing, N. Mathews, S. Y. Sun, S. S. Lim, Y. M. Lam, M. Grätzel, S. Mhaisalkar and T. C. Sum, *Science*, 2013, **342**, 344–347.
19 D. Q. Bi, W. Tress, M. Ibrahim Dar, P. Gao, J. S. Luo, C. Renevier, K. Schenk, A. Abate, F. Giordano, J.-P. Correa Baena, J.-D. Decoppet, S. M. Zakeeruddin, M. K. Nazeeruddin, M. Grätzel and A. Hagfeldt, *Sci. Adv.*, 2016, DOI: 10.1126/sciadv.1501170.
20 Q. Chen, H. Zhou, Z. Hong, S. Luo, H. S. Duan, H. H. Wang, Y. Liu, G. Li and Y. Yang, *J. Am. Chem. Soc.*, 2014, **136**, 622–625.
21 T. Du, N. Wang, H. J. Chen, H. Lin and H. C. He, *ACS Appl. Mater. Interfaces*, 2015, **7**, 3382–3388.
22 M. R. Leyden, L. K. Ono, S. R. Raga, Y. Kato, S. H. Wang and Y. B. Qi, *J. Mater. Chem. A*, 2014, **2**, 18742–18745.
23 C. W. Chen, H. W. Kang, S. Y. Hsiao, P. F. Yang, K. M. Chiang and H. W. Lin, *Adv. Mater.*, 2014, **26**, 6647–6652.
24 H. Hu, D. Wang, Y. Y. Zhou, J. L. Zhang, S. L. Lv, S. P. Pang, X. Chen, Z. H. Liu, N. P. Padtureb and G. L. Cui, *RSC Adv.*, 2014, **4**, 28964–28967.
25 Q. Dong, Y. Yuan, Y. Shao, Y. Fang, Q. Wang and J. Huan, *Energy Environ. Sci.*, 2015, **8**, 2464–2470.
26 W. Zhang, M. Saliba, D. T. Moore, S. K. Pathak, T. Hörantner, M. K. Stergiopoulos, S. D. Stranks, G. E. Eperon, J. A. Alexander-Webber, A. Abate, A. Sadhanala, S. H. Yao, Y. L. Chen, R. H. Friend, L. A. Estroff, U. Wiesner and H. J. Snaith, *Nat. Commun.*, 2014, **6**, 6412.
27 D. W. de Quilettes, S. M. Vorpahl, S. D. Stranks, H. Nagaoka, G. E. Eperon, M. E. Ziffer, H. J. Snaith and D. S. Ginger, *Science*, 2015, **348**, 683.
28 C. Bi, Y. B. Yuan, Y. J. Fang and J. S. Huang, *Adv. Energy Mater.*, 2015, **5**, 1401616.
29 H. J. Snaith, A. Abate, J. M. Ball, G. E. Eperon, T. Leijtens, N. K. Noel, S. D. Stranks, J. T.-W. Wang, K. Wojciechowski and W. Zhang, *J. Phys. Chem. Lett.*, 2014, **5**, 1511–1515.
30 H.-S. Kim and N.-G. Park, *J. Phys. Chem. Lett.*, 2014, **5**, 2927–2934.
31 W. Tress, N. Marinova, T. Moehl, S. M. Zakeeruddin, M. K. Nazeeruddin and M. Grätzel, *Energy Environ. Sci.*, 2015, **8**, 995–1004.
32 Y. H. Shao, Z. G. Xiao, C. Bi, Y. B. Yuan and J. S. Huang, *Nat. Commun.*, 2014, **5**, 5784.
33 J. Wei, Y. C. Zhao, H. Li, G. B. Li, J. L. Pan, D. S. Xu, Q. Zhao and D. P. Yu, *J. Phys. Chem. Lett.*, 2014, **5**, 3937–3945.
34 R. S. Sanchez, V. Gonzalez-Pedro, J.-W. Lee, N.-G. Park, Y. S. Kang, I. Mora-Sero and J. Bisquert, *J. Phys. Chem. Lett.*, 2014, **5**, 2357–2363.
35 A. H. Ip, L. N. Quan, M. M. Adachi, J. J. McDowell, J. Xu, D. Ha Kim and E. H. Sargent, *Appl. Phys. Lett.*, 2015, **106**, 143902.
36 S. Yuan, Z. Qiu, H. Zhang, H. Gong, Y. Hao and B. Cao, *Appl. Phys. Lett.*, 2016, **108**, 033904.